7

CHAPTER 7: MATHEMATICAL OPTIMISATION OF LAMINAR-FORCED CONVECTION HEAT TRANSFER THROUGH A VASCULARISED SOLID WITH COOLING CHANNELS[5]

7.1. INTRODUCTION

This section develops numerically and analytically the geometric optimisation of parallel cooling channels in forced convection for a vascularised material with the localised self-cooling property subjected to a heat flux on one side. This is done in such a way that the peak temperature was minimised at every point in the solid body. The self-cooling ability of vascularised material to bathe volumetrically at every point of a solid body gave rise to the name 'smart material'.

Constructal theory ideally helps in the vascularisation of the smart material structure by morphing the flow architecture configuration to provide easier and greater access of flow through it.

This work is follows on that of Kim *et al.* [128], who theoretically and numerically analysed vascularised materials with heating from one side and coolant forced from

---

[5] This research section is published in part: O.T. Olakoyejo, T. Bello-Ochende and J.P Meyer, "Mathematical optimisation of laminar-forced convection heat transfer through a vascularised solid with square channels", *International Journal of Heat and Mass Transfer*, Vol. 55, 2012, pp. 2402-2411.

the other side. They did the analysis for parallel plates and cylindrical channel configurations in an attempt to find the channel configurations that minimised the non-uniform temperature distribution of a vascularised solid body. The work in this section focuses on the mathematical optimisation of laminar-forced convection heat transfer through a vascularised solid with square channels. It examines the optimisation of a fixed and finite global volume of solid material with an array of square cooling channels. A uniform heat flux applied from one side and the cooling fluid was forced through the channels from the opposite direction with a specified pressure difference. The structure had three degrees of freedom as design variables: the elemental volume, the channel's hydraulic diameter and channel-to-channel spacing. The objective was to build a smaller construct to form part of a larger construct body with a self-cooling function, which would lead to the minimisation of the global thermal resistance or, inversely, the maximisation of the heat transfer rate density (the total heat transfer rate per unit volume). This would be achieved by designing the body in a vascularised manner and by forcing a coolant to the heated spot in a fast and efficient way so as to significantly reduce the peak temperature at any point inside the volume that needs cooling.

We started the optimisation process by carrying out numerical solutions under a fixed global volume of solid material, but the elemental volume was allowed to morph. A gradient-based optimisation algorithm (DYNAMIC-Q) (see Chapter 4), coupled with the numerical CFD and mesh generation packages, was used to determine the optimal

geometry that gave the lowest thermal resistance. This optimiser adequately handled the numerical objective function obtained from numerical simulations of the fluid flow and heat transfer.

We later developed an analytical solution based on the application of the intersection of asymptotes method and scale analysis to prove the existence of an optimal geometry that would minimise the peak temperature and global thermal resistance of this vascularised material.

The numerical results obtained were in agreement with a theoretical formulation for this vascularised solution using scale analysis and the intersection of asymptotes method. The effect of material properties on the minimum thermal resistance and optimised internal configuration was also studied.

7.2. COMPUTATIONAL MODEL

The schematic diagram of the physical configuration is shown in Figure 7.1. The system consists of a solid body of fixed global volume V, which is heated with uniform heat flux q'' on the left side. The body is cooled by forcing a single-phase cooling fluid (water) from the right side through the parallel cooling channels.

The flow is driven along the length L of the square channel ($w_c = h_c$) with a fixed pressure difference ΔP in a transverse and counter-direction to the heat flux. An elemental volume (see Figure 7.2) consisting of a cooling channel and the surrounding solid was used for analysis because it was assume that heat distribution would occur symmetrically on the left side of the structure. The heat transfer in the elemental volume is a conjugate problem, which combines heat conduction in the solid and the convection in the working fluid.
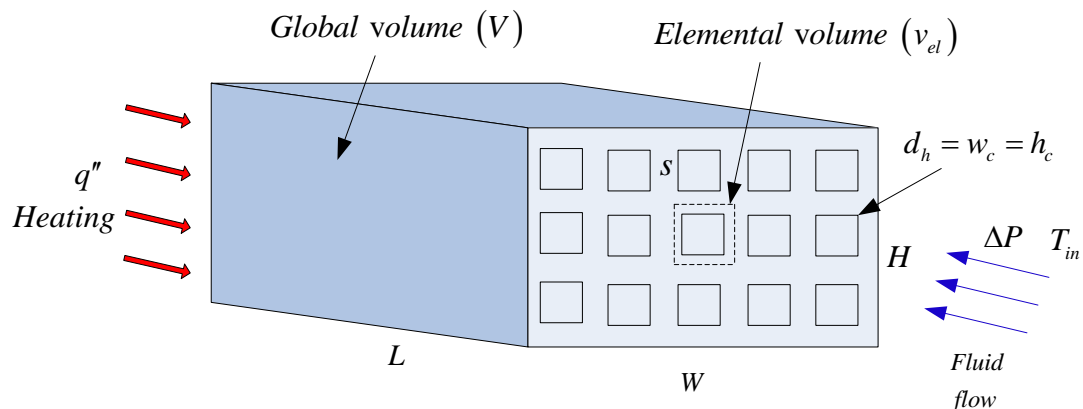
Figure 7. 1 : Three-dimensional parallel square channels across a slab with heat flux from one side and forced flow from the opposite side

7.2.1. Numerical procedure

Figure 7.2 shows that an elemental volume v_{el} constraint is considered to be composed of an elemental cooling channel of hydraulic diameter d_h ($d_h = w_c = h_c$). The surrounding solid of thickness s (the spacing between channels) is defined as

$$w = h \tag{7.1}$$

The elemental volume is

$$v_{el} = w^2 L \tag{7.2}$$

and the width of an elemental volume is

$$w = d_h + s \tag{7.3}$$

Therefore, the number of channels in the structure arrangement can be defined as:

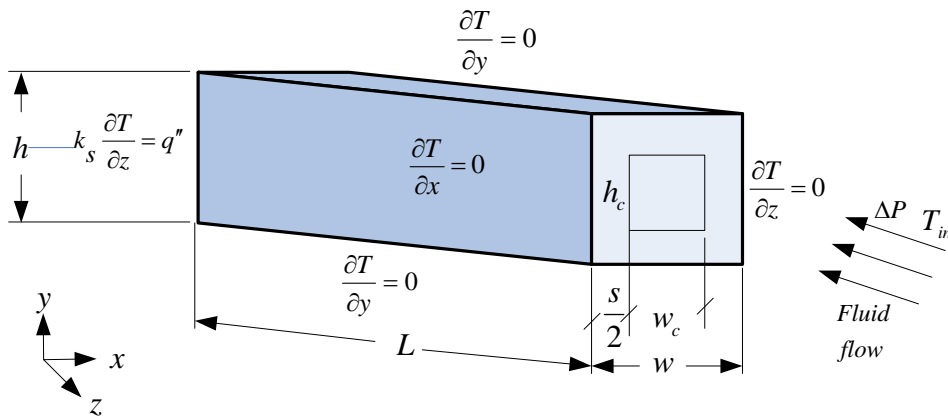$$N = \frac{HW}{\left(d_h + s\right)^2} \tag{7.4}$$

Figure 7. 2 : The boundary conditions of the three-dimensional computational domain of the elemental volume

and the void fraction or porosity of the unit structure can be defined as

$$\phi = \frac{v_c}{v_{el}} = \left(\frac{d_h}{w}\right)^2 \tag{7.5}$$

The fundamental problem under consideration is the numerical optimisation of the channel hydraulic diameter, d_h, and the channel spacing, s, which corresponds to the minimum resistance of a fixed volume for a specified pressure drop. The optimisation is evaluated from the analysis of the extreme limits of $0 \leq d_h \leq \infty$ and the extreme limits of $0 \leq s \leq \infty$. The optimal values of the design variables within the prescribed interval of the extreme limits exhibit the minimum thermal resistance.

The temperature distribution in the elemental volume was determined by solving the equation for the conservation of mass and momentum Equations (Equations (3.1) to (3.7) of Chapter 3) numerically. A section of the discretised three-dimensional computational domain of the elemental volume is shown in Figure 7.3. The cooling fluid was water, which was forced through the cooling channels by a specified pressure difference ΔP across the axial length of the structure. The working fluid is water and is assumed to be in single phase, steady and Newtonian with constant properties.

The energy equation for the solid part of the elemental volume can be written as

$$k_s \nabla^2 T = 0 \tag{7.6}$$

The continuity of the heat flux at the interface between the solid and the liquid is given as:

$$k_s \left. \frac{\partial T}{\partial n} \right|_w = k_f \left. \frac{\partial T}{\partial n} \right|_w \tag{7.7}$$

A no-slip boundary condition is specified for the fluid at the wall of the channel,

$$\vec{u} = 0 \tag{7.8}$$

At the inlet ($z = L$),
$$u_x = u_y = 0 \tag{7.9}$$

$$T = T_{in} \tag{7.10}$$

$$P = \frac{Be\alpha\mu}{L^2} + P_{out} \tag{7.11}$$

where, the Bejan number [182, 183], *Be,* is the dimensionless pressure difference and given as:

$$Be = \frac{\Delta P L^2}{\mu \alpha_f} \tag{7.12}$$

and

$$\alpha_f = \frac{k_f}{\rho_f C_{Pf}} \tag{7.13}$$

At the outlet ($z = 0$), the pressure is prescribed as zero normal stress

$$P_{out} = 1 \, atm \tag{7.14}$$

At the left side of the wall, the thermal boundary condition that is imposed is assumed to be:

$$q'' = k_s \frac{\partial T}{\partial z} \qquad (7.15)$$

while at the solid boundaries, the remaining outside walls and the plane of symmetry

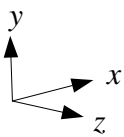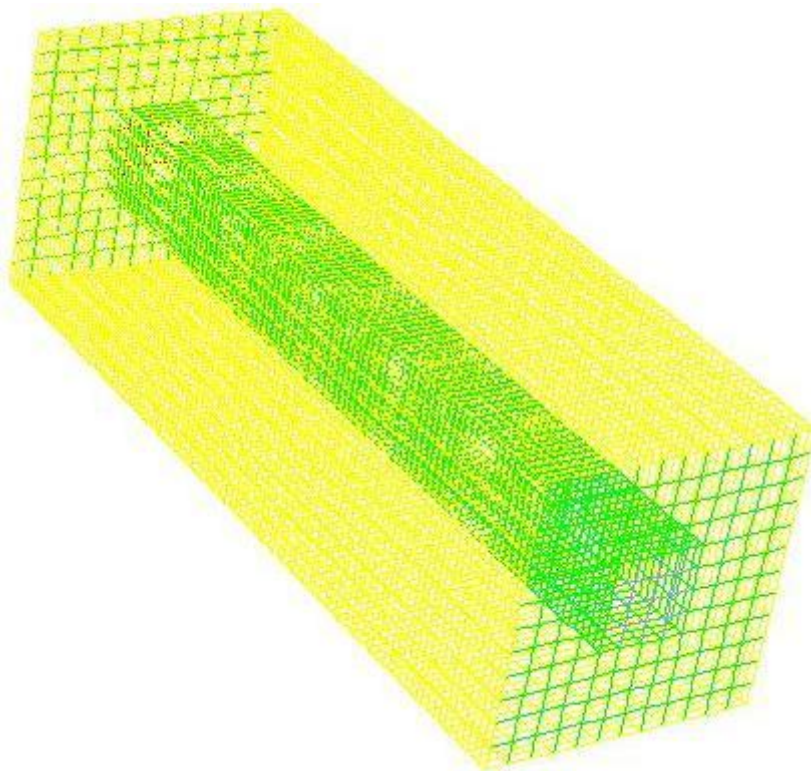are modelled as adiabatic as shown in Figure 7.2

$$\nabla T = 0 \qquad (7.16)$$

Figure 7. 3 : A section of the discretised 3-D computational domain of the elemental solid-fluid volume considered for the simulation

The measure of performance is the minimum global thermal resistance, which could be expressed in a dimensionless form as:

$$R_{\min} = \frac{k_f \left(T_{\max} - T_{in}\right)_{\min}}{q''L} \tag{7.17}$$

and it is a function of the optimised design variables and the peak temperature.

$$R_{\min} = f\left(d_{h_{opt}},\ v_{el_{opt}},\ T_{\max_{\min}}\right) \tag{7.18}$$

$R_{\min}$ is the minimised thermal resistance for the optimised design variables. The inverse of $R_{\min}$ is the optimised overall global thermal conductance.

The effect of material properties is later taken into consideration by the ratio of the thermal conductivities

$$k_r = \frac{k_s}{k_f} \tag{7.19}$$

7.3. NUMERICAL PROCEDURE

The simulation work began by fixing the length of the channel, prescribed pressure difference, porosity, heat flux and material properties. We used varying values of the hydraulic diameter of the channel to identify the best (optimal) internal configuration that minimised the peak temperature. The numerical solution of the continuity, momentum and energy equations (Equations (3.1) to (3.7)) along with the boundary conditions (Equations (7.6) to (7.15)) was obtained by using a three-dimensional commercial package Fluent™ [199] which employs a finite volume method. The

details of the method are m explained by Patankar [203]. Fluent™ [199], was coupled with the geometry and mesh generation package Gambit [201] using MATLAB [219] to allow the automation and running of the simulation process. After the simulation had converged, an output file was obtained containing all the necessary simulation data and results for the post-processing and analysis. The computational domain was discretised using hexahedral/wedge elements. A second-order upwind scheme was used to discretise the combined convection and diffusion terms in the momentum and energy equations. The SIMPLE algorithm was subsequently employed to solve the coupled pressure-velocity fields of the transport equations. The solution is assumed to have converged when the normalised residuals of the mass and momentum equations fall below 10^{-6} while the residual convergence of energy equation was set to less than 10^{-10}. The number of grid cells used for the simulations varied for different elemental volume and porosities. However, grid independence tests for several mesh refinements were carried out to ensure the accuracy of the numerical results. The convergence criterion for the overall thermal resistance as the quantity monitored was

$$\gamma = \frac{\left|(T_{max})_i - (T_{max})_{i-1}\right|}{\left|(T_{max})_i\right|} \leq 0.001 \tag{7.20}$$

where i is the mesh iteration index. The mesh was more refined as i increased. The $i-1$ mesh was selected as a converged mesh when the criterion (7.20) was satisfied.

7.4. GRID ANALYSIS AND CODE VALIDATION

To ensure accurate results, several grid independence test were conducted until a mesh size with negligible changes in peak temperature was obtained.

Table 7.1 shows the grid independence test performed for the case where $d_h = 400$ µm and $\phi = 0.2$ for $Be = 10^8$. Computational cell densities of 3 675, 5952, 11 200 and 20 160 were used for the grid independence test. Almost identical results were predicted when 5 952 and 11 200 cells were used. Therefore, a further increase in the cell density beyond 11 200 would have a negligible effect on the results.

Table 7. 1: **Grid independence study with** $d_h = 400\mu$m **and** $\phi = 0.2$ **for** $Be = 10^8$

Number of nodes	Number of cells	T_{max}	$\gamma = \dfrac{\left|(T_{max})_i - (T_{max})_{i-1}\right|}{\left|(T_{max})_i\right|}$
5 456	3 675	33.09371	-
8 718	5 952	32.79123	0.009194
15 005	11 200	32.772	0.000587
26 609	20 160	32.67453	0.002983

The validation of the numerical simulation was carried out by comparing the present simulation with that of Kim *et al* [128] for a cylindrical configuration as shown in Figure 7.4 for the case where $\phi = 0.1$ and $k_r = 10$. The curves were found to be similar in trend and the solutions were in good agreement with a deviation of less than 7%.
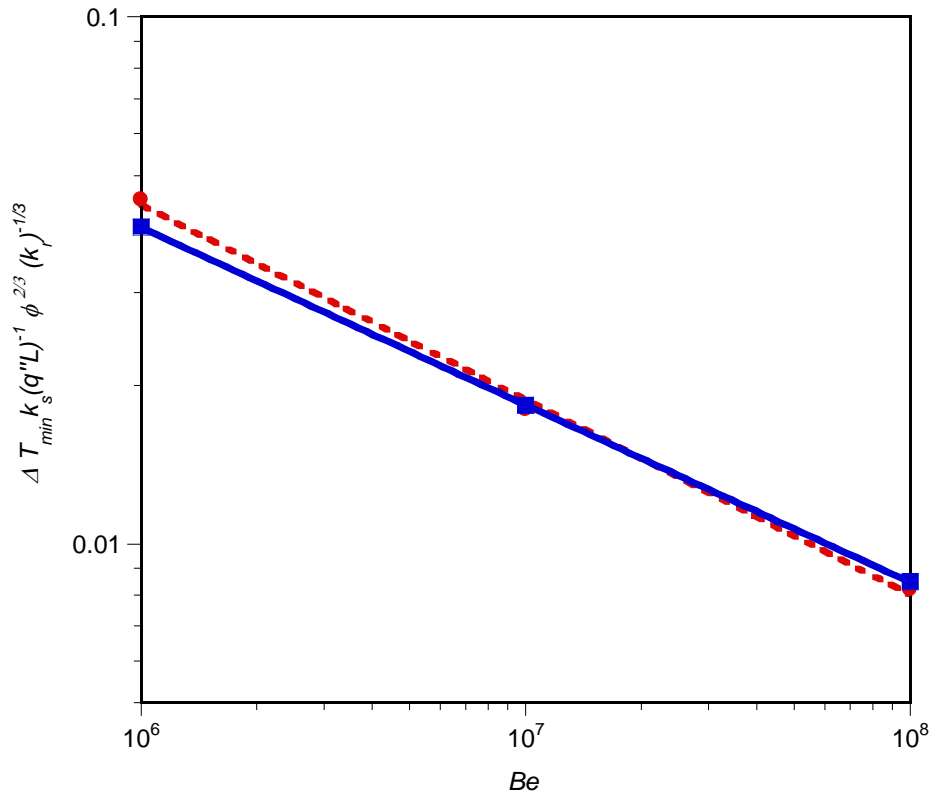
Figure 7. 4 : Comparison of the results of the present numerical study with those of Kim *et al.* [128] for $\phi = 0.1$ and $k_r = 10$

7.5. NUMERICAL RESULTS

In this section, we present results for the case when the channel hydraulic diameter (or channel width/height) was in the range of 0.1 mm to 1.5 mm and the porosities ranged between $0.1 \leq \phi \leq 0.3$, while a fixed length of $L = 10$ mm and fixed applied dimensionless pressure differences of $Be = 10^8$. The thermal conductivity of the solid structure (stainless steel) was 16.27 W/m.K; and the heat flux supplied at the left wall was 100 kW/m^2. The thermo-physical properties of water [202] used in this study

were based on water at 300 K and the inlet water temperature was fixed at this temperature.

Figures 7.5 and 7.6 show the existence of an optimum hydraulic diameter and elemental volume size in which the peak temperature is minimised at any point in the channel for the square configuration studied. According to Figure 7.5 the peak temperature is a function of the channel hydraulic diameter. It shows that there exists an optimal channel hydraulic diameter, which lies in the range $0.01 \leq d_h/L \leq 0.05$ minimising the peak temperature. Also, the elemental volume of the structure has a strong effect on the peak temperature as shown in Figure 7.6. The minimum peak temperature is achieved when the optimal elemental volume is in the range $0.05 \text{ mm}^3 \leq v_{el} \leq 8 \text{ mm}^3$. This indicates that the global peak temperature decreases as the design variables (hydraulic diameter and elemental volume) increase, or the global peak temperature decreases as the design variables decrease until it gets to the optimal design values. Therefore, any increase or decrease in the design variable beyond the optimal values indicates that the working fluid is not properly engaged in the cooling process, which is detrimental to the global performance of the system. The results show that the optimal arrangement of the elemental volume for the entire structure at this fixed pressure difference should be very small in order to achieve a better cooling. Figures 7.5 and 7.6 also show that porosity has a significant effect on the peak temperature. The best cooling occurs at the highest porosity. Thus, as the porosity increases, the peak temperature decreases.
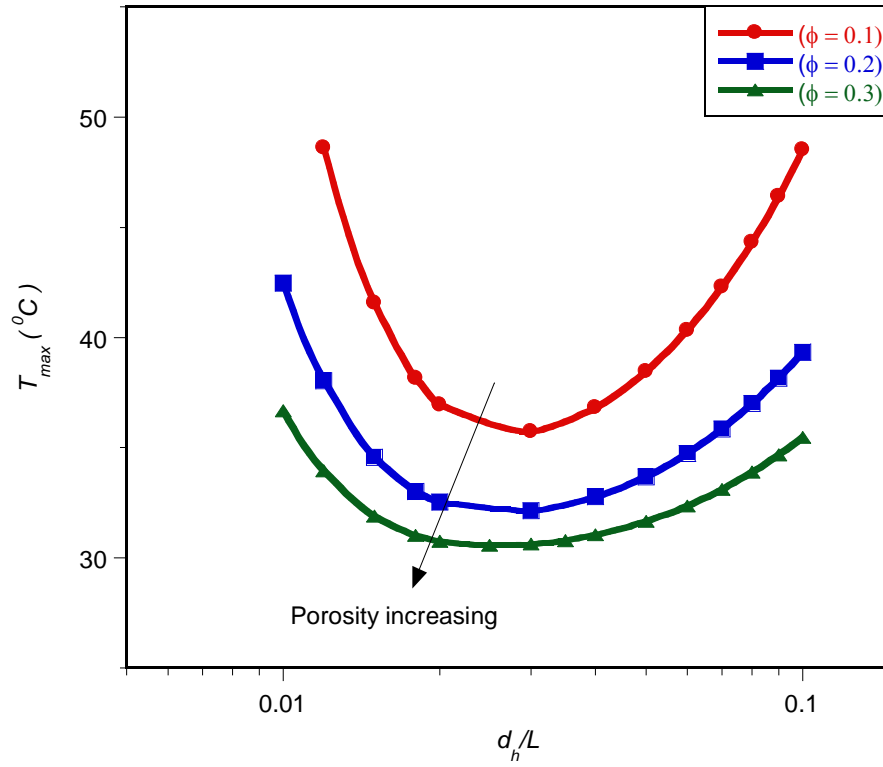
Figure 7. 5 :   Effect of the optimised dimensionless hydraulic diameter d_h on the peak temperature at $Be = 10^8$
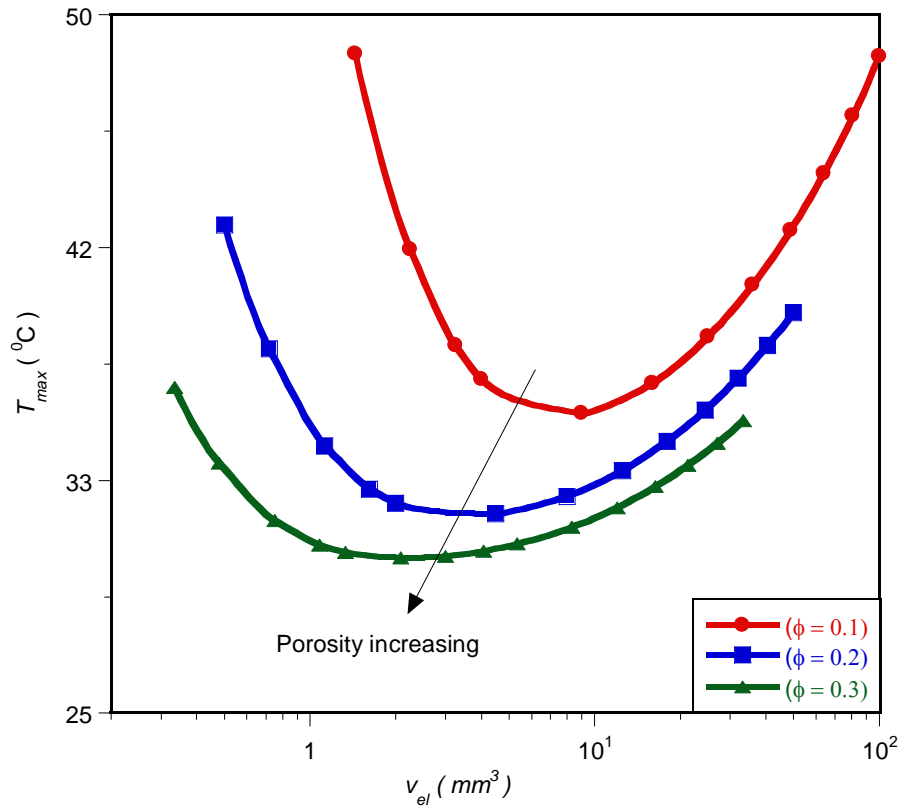
Figure 7. 6 :   Effect of the optimised elemental volume on the peak temperature at Be = 10^8

7.6. MATHEMATICAL FORMULATION OF THE OPTIMISATION PROBLEM

In this section, we introduce an optimisation algorithm that will search and identify the design variables at which the system will perform at an optimum. A numerical algorithm, Dynamic-Q [208], was employed and incorporated into the finite volume solver and grid (geometry and mesh) generation package by using MATLAB code for greater efficiency and better accuracy in determining the optimal performance.

181

7.6.1. Optimisation problem and design variable constraints

The optimisation technique described above was applied to the models described in Section 7.2. The constraint ranges for the optimisation are:

$$0.1 \leq \phi \leq 0.3 \tag{7.21}$$

$$0 \leq w \leq L \tag{7.22}$$

$$0 \leq d_h \leq w \tag{7.23}$$

$$0 \leq s \leq w \tag{7.24}$$

The design and optimisation technique involves the search for and identification of the best channel layout that minimises the peak temperature, T_{max}, so that the minimum thermal resistance between the fixed volume and the cooling fluid is obtained as the desired objectives function. The hydraulic diameter, channel spacing and elemental volume of the square configuration were considered as design variables. A number of numerical optimisations and calculations were carried out within the design constraint ranges given in Equations (7.21) to (7.24). The results are presented in the next section to show the optimal behaviour of the entire system. The optimisation process was repeated for applied dimensionless pressure differences Be from 10^5 to 10^9.

7.6.2. Mathematical statement of the optimisation problem

The variables chosen for the mathematical statement are

$$x_1 = d_h \tag{7.25}$$

$$x_2 = w \tag{7.26}$$

Substituting Equations (7.25) to (7.26) for Equations (7.21) to (7.24) results in the objective and constraints functions given in Equations (7.27) to (7.29). The inequality functions $g_1(\mathrm{x})$ and $g_2(\mathrm{x})$ are derived from the porosity constraint of Equation (6.5). The mathematical statement of the optimisation problem is then written as:

$$f(x) = T_{\max} \tag{7.27}$$

$$g_1(x) = 0.1 x_2^{\,2} - x_1^{\,2} \leq 0 \tag{7.28}$$

$$g_2(x) = x_1^{\,2} - 0.2 x_2^{\,2} \leq 0 \tag{7.29}$$

7.6.3. Parameterisation of geometry and automation of the optimisation process

Since a large number of CFD simulations were performed, the geometry and mesh generation are parameterised in similar way as those described in Chapter 6. This allowed GAMBIT [201] scripts to be automatically generated. The optimisation problem was done automatically by coupling together the computational fluid dynamics package- FLUENT[199] and the geometry and mesh generation package GAMBIT [201] with the mathematical optimisation algorithm by using MATLAB [219] to allow the automation, mesh generation and running of the simulation process.

The values in the parametric GAMBIT file were changed through MATLAB code, and then the procedure was re-run to generate a new set of geometric modelling and mesh generations for post-processing. This cycle continued until convergence occurred with the step size and function value convergence tolerances set at 10^{-4} and 10^{-8} respectively. Figure 6.10 provides a flow chart of the automated optimisation process. The peak temperature was found and equated to the objective function.

Appendix B.6 shows the parametric GAMBIT file for geometry of the vascularised square cooling channels of Figure 7.1. Appendices A and C show the optimisation algorithm file and the FLUENT journal file respectively for the running of the simulation.

7.6.4. Sensitivity analysis of the selection of forward differencing step size

As discussed in Chapter 4. 6, the fact that noise exists in any simulation made it essentially to carefully choose a step size Δx to be used in the differencing scheme. This step size had to totally minimise the noise and gives an accurate representation of the global gradient of the function. A sensitivity analysis was performed by selecting different values of the step size of design variables that gave a smooth objective function and could later be used as candidate step size. This candidate step size was then verified by running the optimisation program with various starting guesses and

checking for any discrepancies in the final solution. Figure 7.7 shows a graph of peak temperature as a function of cooling channel width with step sizes of 10^{-6} and 10^{-4}. Although, different values of the step size of cooling channel width as design variable considered are 10^{-6}, 10^{-5}, 10^{-4} and 10^{-3}
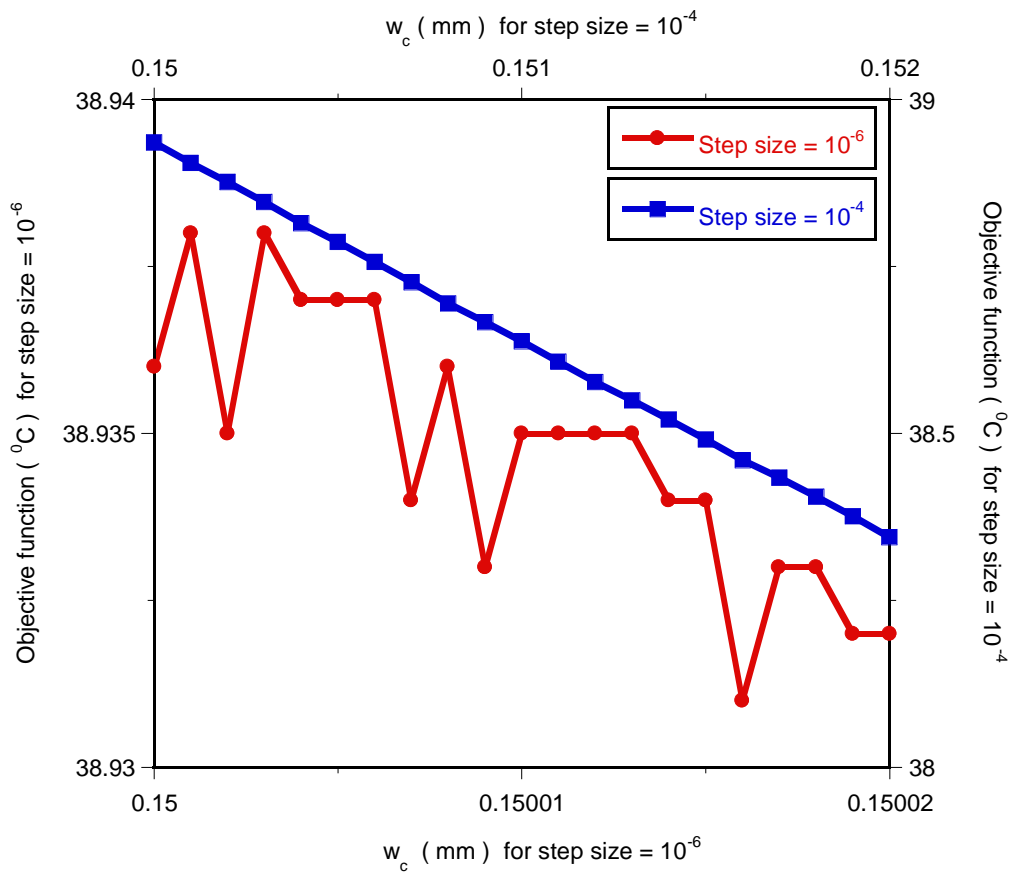

Figure 7. 7 : Plotting peak temperatures for different channel width values with step sizes of 10^{-6} and 10^{-4}

A step size of 10^{-4} gave a smooth continuous function of maximum peak temperature and it indeed proved to be an ideal forward differencing scheme step size for other design variables.

Figure 7.8 shows a graph of peak temperature as a function of channel spacing with the chosen candidate step size of 10^{-4}.
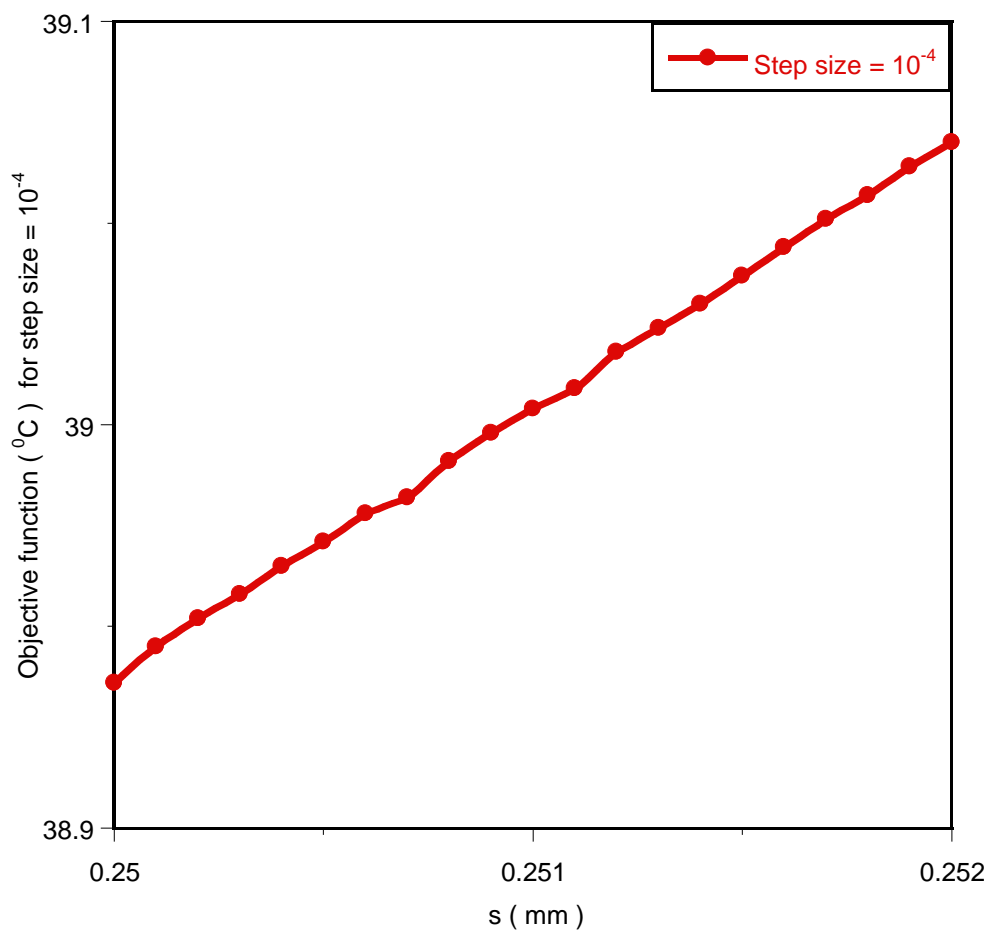
Figure 7. 8 : Plotting peak temperatures for different channels-spacing values with a step size of 10^{-4}

7.7. OPTIMISATION RESULTS

7.7.1. Effect of pressure difference on optimised geometry and minimised thermal resistance

Figure 7.9 shows the effect of the minimised thermal resistance as a function of applied dimensionless pressure difference. Minimised thermal resistance decreases as the applied dimensionless pressure difference and porosity increase. Figure 7.10 shows that the optimal hydraulic diameter decreases as the pressure differences increase and there exists a unique optimal geometry for each of the applied pressure differences. The trend is in agreement with previous work [94].

7.7.2. Effect of material properties on optimised geometry and minimised thermal resistance

The effect of material properties on the minimum thermal resistance and optimised internal configuration was also studied. This was best investigated by numerically simulating conjugate heat transfer in an elemental volume for different values of thermal conductivity ratio. The numerical simulations follow the same procedure that was discussed earlier to show the existence of an optimal geometry.
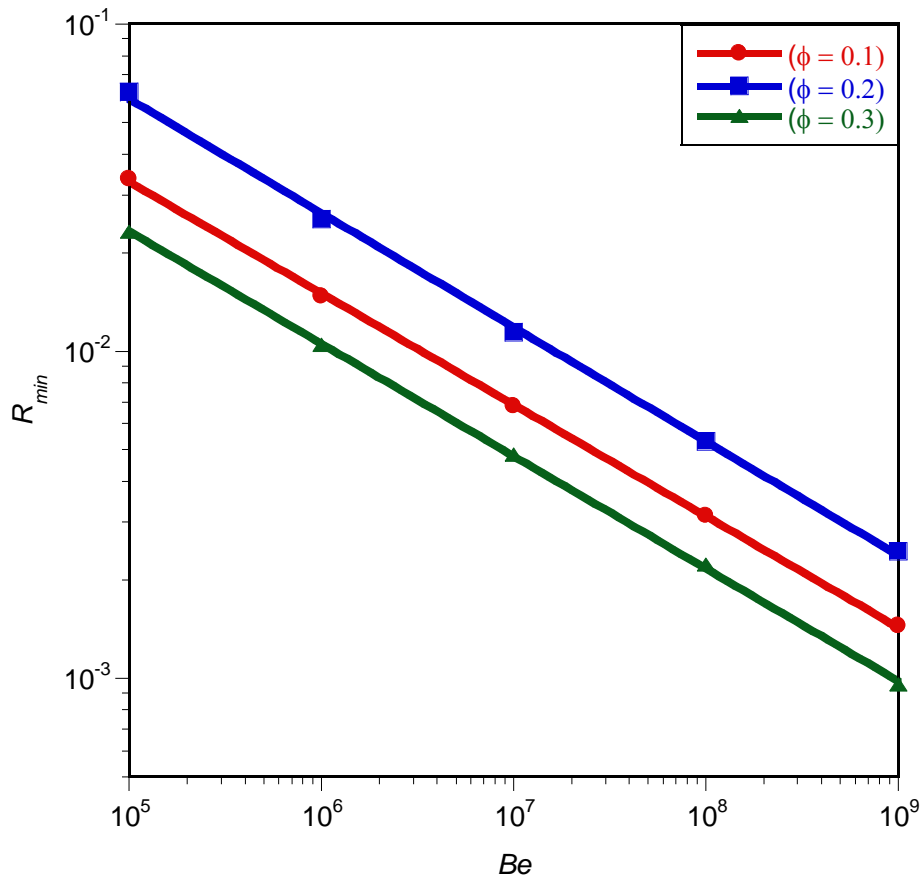
Figure 7. 9 : Effect of dimensionless pressure difference on the dimensionless global thermal resistance
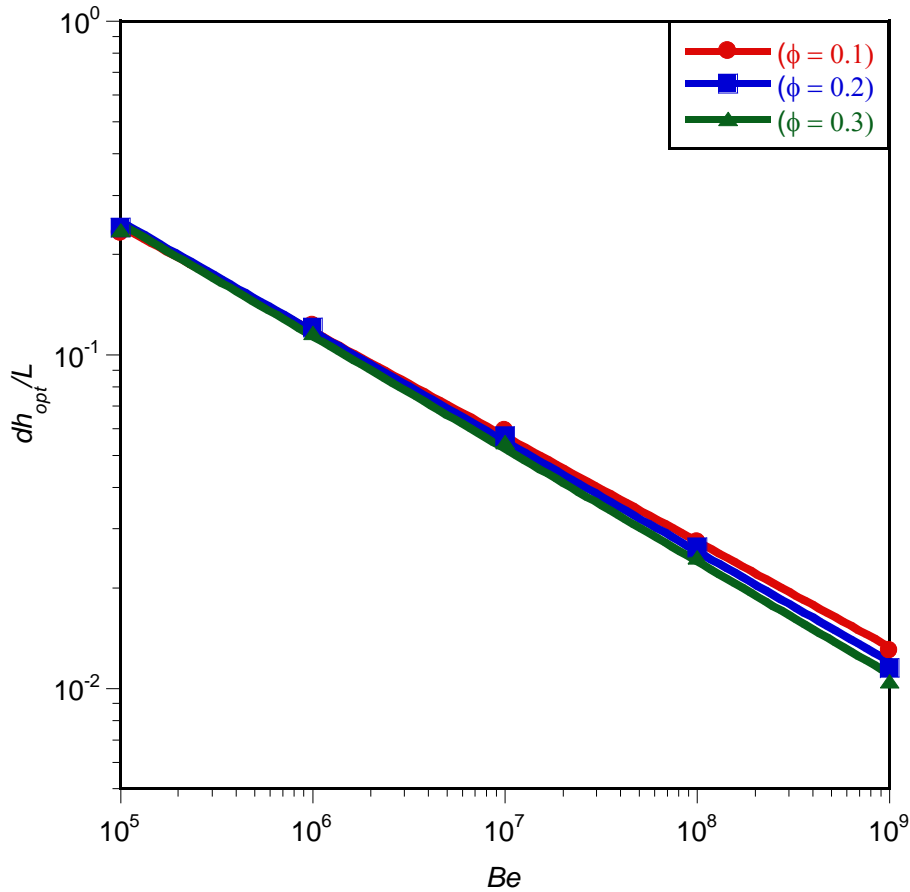
Figure 7. 10 : Effect of dimensionless pressure difference on the optimised hydraulic diameter

We started the simulation by fixing $\phi = 0.2$, $Be = 10^8$ and $k_r = 10$ as well as and $k_r = 100$. We then varied the hydraulic diameter and the elemental volume until we got the minimum peak temperature. Figure 7.11 shows that an optimal geometry exists at different thermal conductivity ratios and that minimum peak temperatures are achieved when k_r is high.
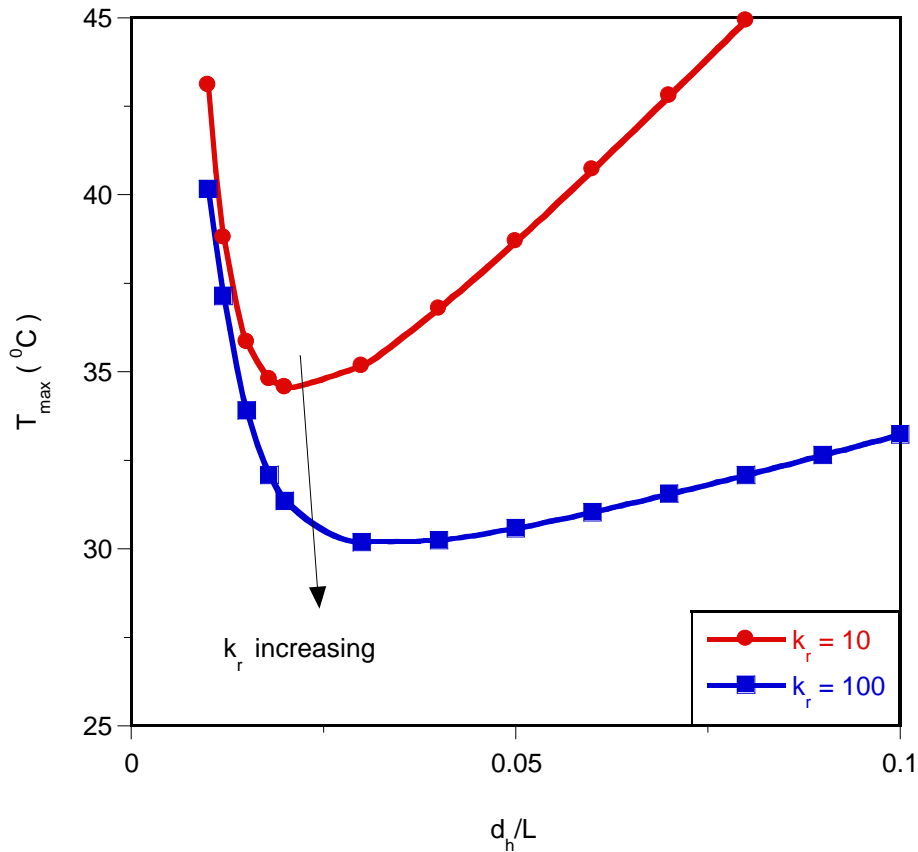
Figure 7. 11 : Effect of a thermal conductivity ratio, k_r , on the peak temperature at a Bejan number of 10^8 and porosity of 0.2

We later performed an optimisation process to determine the best geometry that would render the lowest thermal resistance temperature by using the optimisation algorithm. We fixed $\phi = 0.2$ and $Be = 10^8$ for all the design constraint ranges and for different values of thermal conductivity ratios ranging from $k_r = 1$ to $k_r = 10^4$. Figures 7.12 and 7.13 show the effect of the thermal conductivity ratio on the minimised global thermal resistance and the optimised hydraulic diameter at fixed $\phi = 0.2$ and $Be = 10^8$. The minimised thermal resistance decreases as the thermal conductivity ratio

190

increases. This shows that material properties have a strong effect on the thermal resistance. Materials with a high thermal conductivity property reduce the thermal resistance. Figure 7.13 shows that the thermal conductivity ratio has a significant influence on the optimised hydraulic diameter. As the thermal conductivity ratio increases, the optimal hydraulic diameter increases. However, at higher thermal conductivity ratios (say $k_r \geq 4\ 000$), the thermal conductivity has a negligible effect on the minimised thermal resistance and optimised hydraulic diameter.
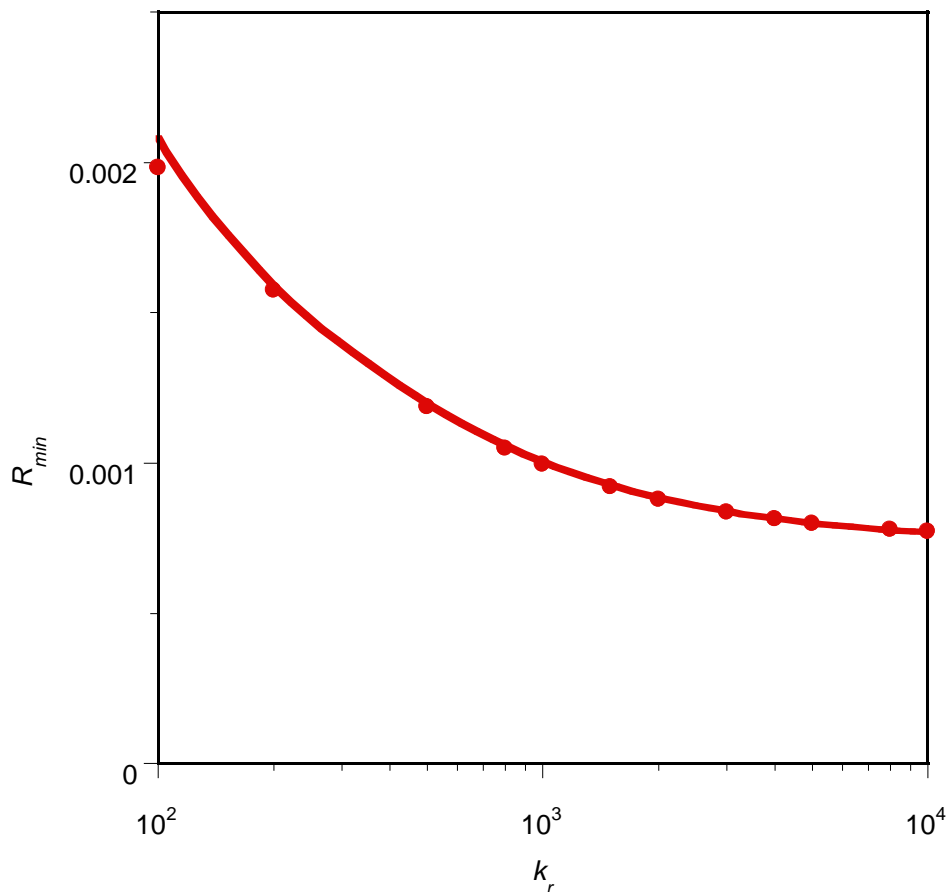
Figure 7. 12 : Effect of a thermal conductivity ratio, k_r on the minimised dimensionless global thermal resistance at Be = 10^8 and porosity of 0.2
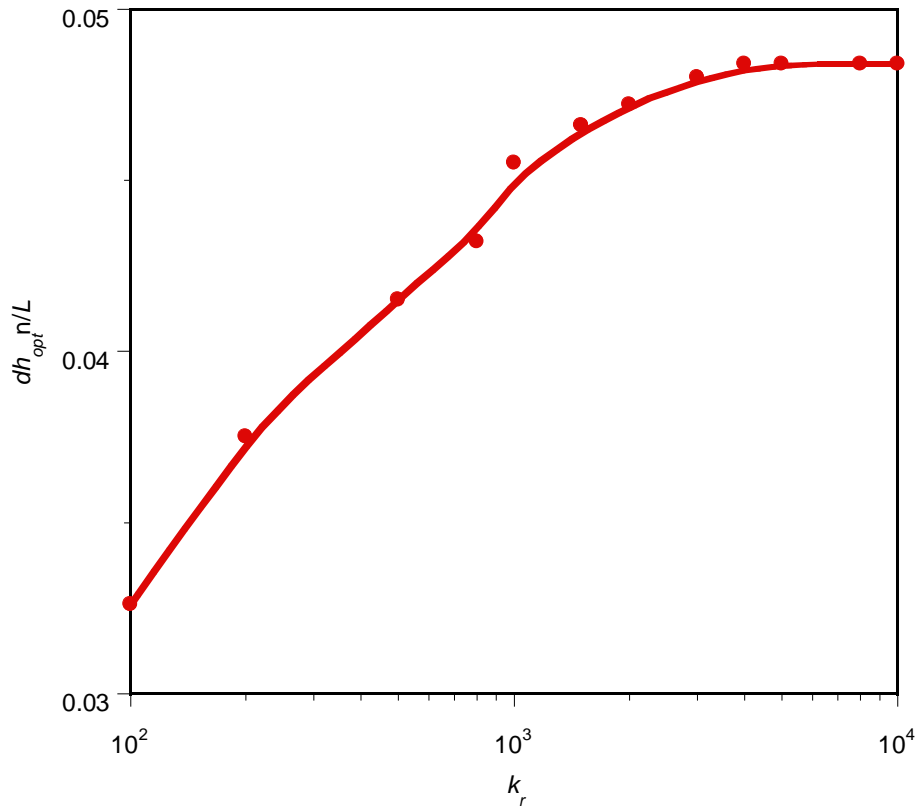
Figure 7. 13 : Effect of thermal conductivity ratio k_r **on the optimised hydraudric diameter at Be = 10^8 and porosity of 0.2**

For applied dimensionless pressure differences ranging from $Be = 10^5$ to 10^9 and $\phi = 0.1$ to 0.2 we repeated the optimisation process for all the design constraint ranges from $k_r = 1$ to 100 so as to determine the global behaviour of the whole system. Figures 7.14 to 7.16 show the effect of the applied dimensionless pressure difference on the minimum thermal resistance and the internal geometry for different values of thermal conductivity ratio and porosity. Figure 7.14 shows that the minimised thermal resistance decreases as the applied dimensionless pressure difference, thermal conductivity ratio and porosity increase. Also, Figures 7.15 and 7.16 show that there

are unique design variables for each applied dimensionless pressure difference, thermal conductivity ratio and porosity.
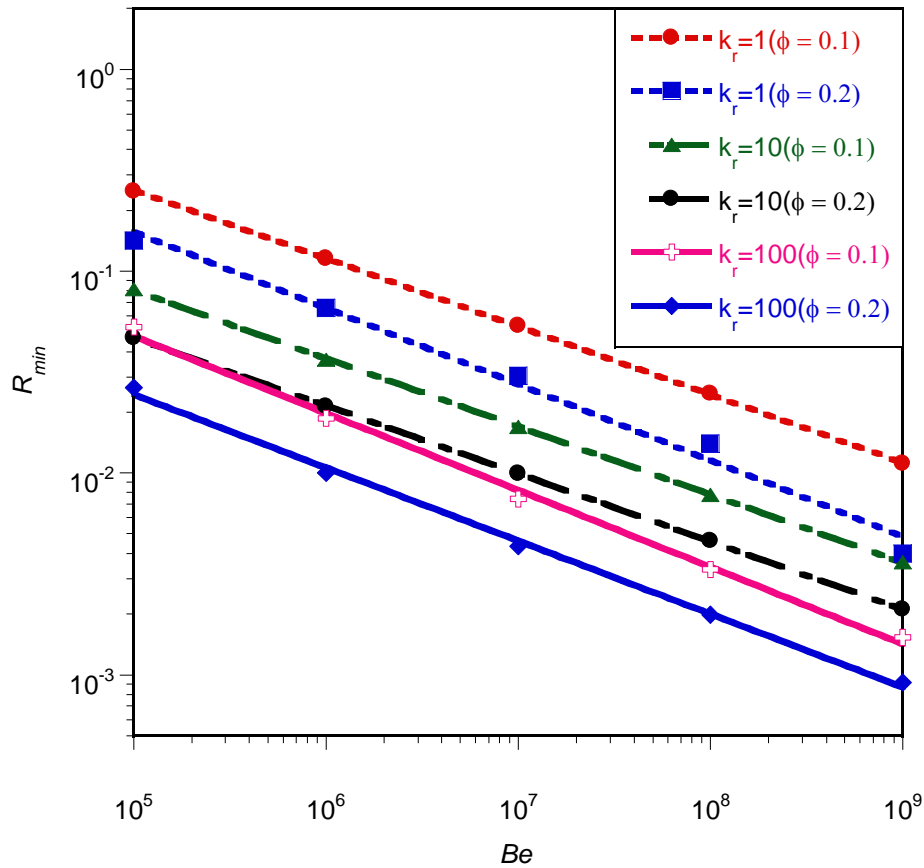

Figure 7. 14 : **Effect of thermal conductivity ratio** k_r **, porosity, and dimensionless pressure difference on the minimised dimensionless global thermal resistance**
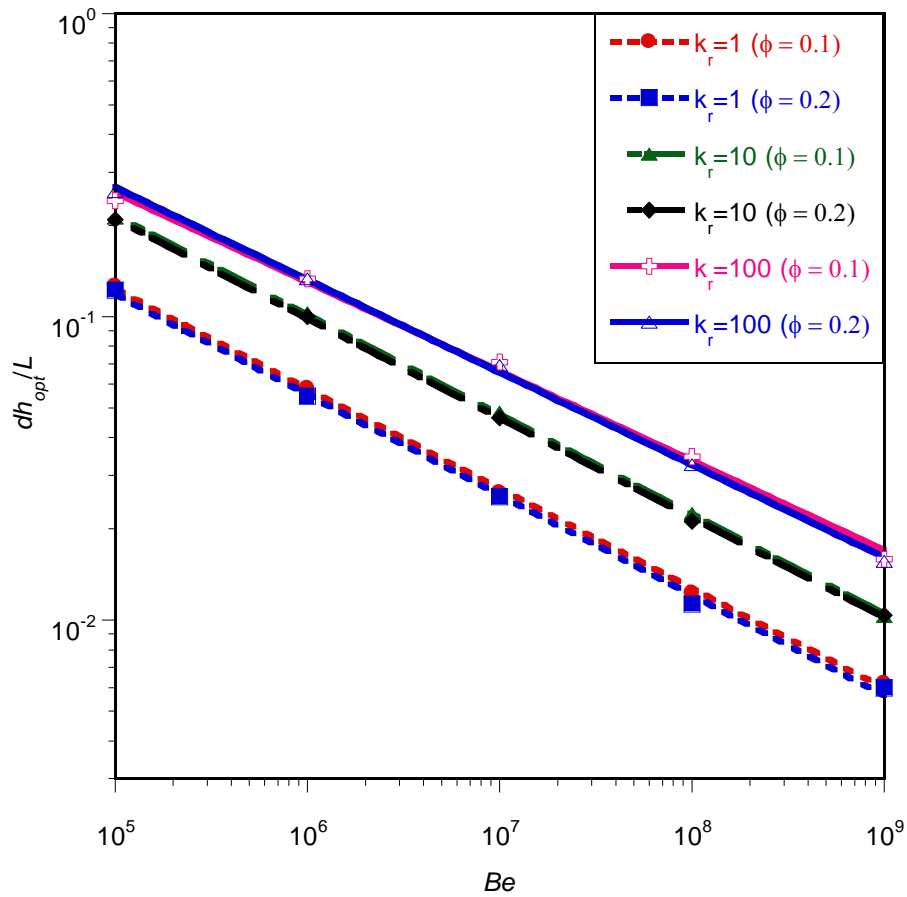
Figure 7. 15 : Effect of thermal conductivity ratio k_r , porosity, and dimensionless pressure difference on the optimised hydraulic diameter
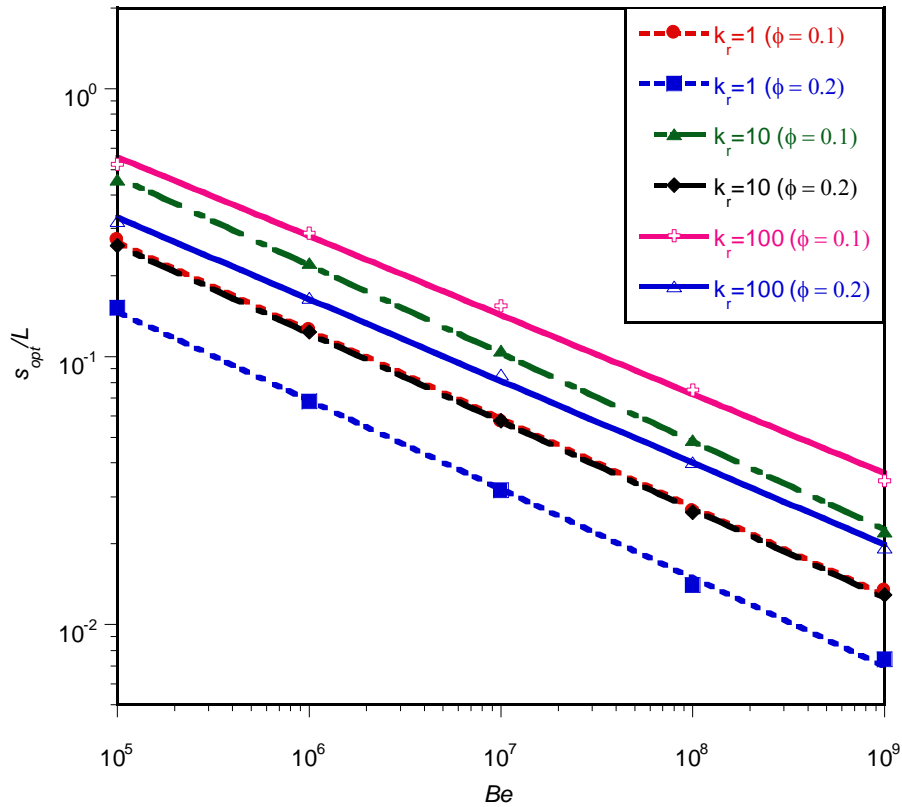
Figure 7.16 : Effect of thermal conductivity ratio k_r, porosity, and dimensionless pressure difference on the optimised channel-spacing

Figures 7.17(a) and 7.17(b) show the temperature contours of the elemental volume and of the inner wall of the cooling channel with cooling fluid, respectively. The blue region indicates the region of low temperature and the red region indicates that of high temperature. The arrow indicates the direction of flow.
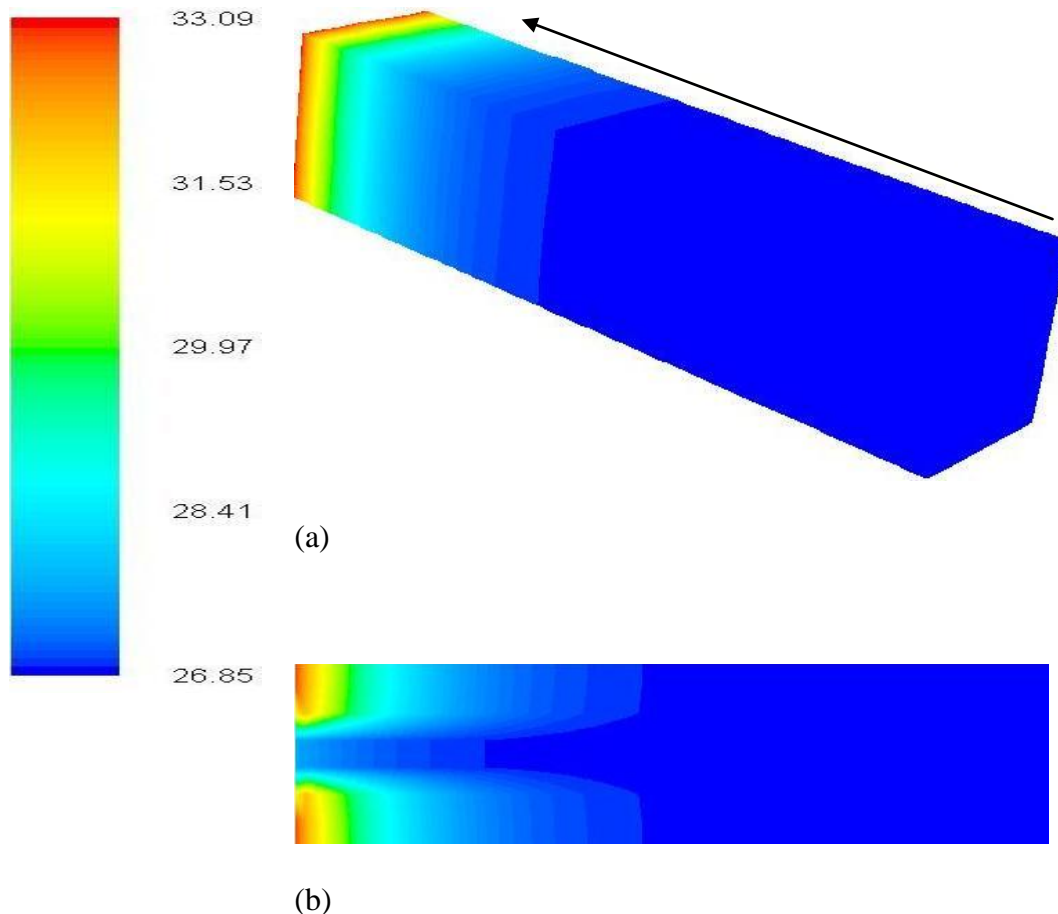
Figure 7. 17: Temperature distributions on (a) the elemental volume and (b) the cooling fluid and the inner wall

7.8. METHOD OF INTERSECTION OF ASYMPTOTES

This section investigated further the numerical solution of the optimisation of flow and heat transfer with the analytical solution. The theoretical analysis for the vascularised configurations followed the application of the intersection of asymptotes method and scale analysis [94, 130, and 218] to prove the existence of an optimal geometry that minimised the peak temperature and global thermal resistance. The

196

method of intersection of asymptotes outlined by Kim *et al.* [130] was used to determine the optimal geometric shape. The objective was to provide the relationship between the global objective function in terms of global thermal resistance, *R*, and the varying hydraulic diameter d_h in the two extremes at $d_h \to 0$ and $d_h \to \infty$. The optimal geometry value $d_{h_{opt}}$ that corresponds to, $R_{\min}$, is located approximately where the two asymptotes intercept.

The following assumptions were made throughout the analysis: inlet temperature and the pressure difference, ΔP, driving the pump are fixed with a uniform flow distribution in all the channels, laminar flow, constant cross-sectional area of the channels, negligible inlet and exit plenum losses and negligible axial conduction. An elemental volume is treated because of the symmetry of the heat distribution.

7.8.1. Extreme limit 1: small channel

Figure 7.18 shows the extreme limit when the channels characteristic dimension is very small and very slender, that is $d_h \to 0$. and $d_h \, \Box \, L$, the length layer is treated as a fluid saturated porous medium with Darcy flow. The flow is fully developed along the length, L. In this extreme limit, the fluid in the channel quickly becomes fully developed flow and the working fluid is overworked.
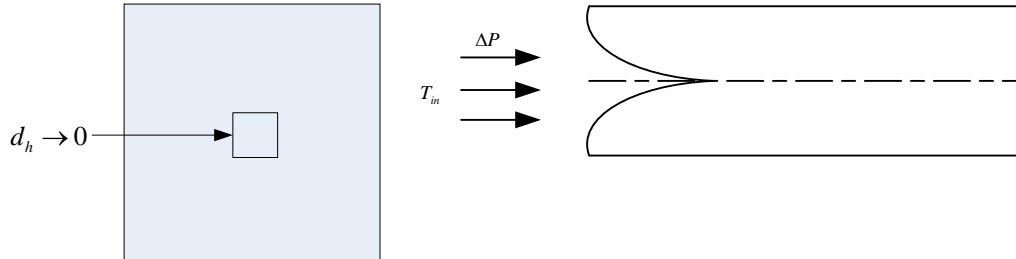
Figure 7. 18 : The extreme limit of the channel's characteristic dimension is very small and very slender, that is $d_h \to 0$ **and** $d_h \square L,$

The average velocity $\bar{u}$ in a uniform volume points in the z direction given as:

$$\bar{u} = \frac{K}{\mu} \frac{\Delta P}{L} \tag{7.30}$$

where, K is the permeability that is associated with Poiseuille flow through

$d_h -$ thin fissures is define [218] as

$$K = \frac{d_h{}^2}{g} \tag{7.31}$$

where g is the porosity function defined [130, 218] as

$$g = \frac{32}{\phi} \tag{7.32}$$

The temperature distribution across the length of the body is obtained by the energy

equation

$$\frac{dT}{dz} = -\frac{\alpha}{u} \frac{\partial^2 T}{\partial z^2} \tag{7.33}$$

This is subject to the flowing boundary conditions

$$q'' = -k_{eff}\frac{dT}{dz} \qquad \text{at } z = 0 \tag{7.34}$$

$$T \to T_{in} \quad \text{as} \quad z \to \infty \tag{7.35}$$

Where, α is the thermal diffusivity of the saturated porous medium and is defined as:

$$\alpha = \frac{k_{eff}}{\rho C_P} \tag{7.36}$$

and k_{eff} is the effective thermal conductivity of the saturated porous medium with the filling fluid in its pores. The fluid-filled spaces are parallel to the direction of heat flow, therefore k_{eff} is defined as:

$$k_{eff} = \phi k_f + (1-\phi)k_s \tag{7.37}$$

The temperature distribution across the length of the body is obtained solving differential Equation (7.33) with the boundary conditions of Equations (7.34) – (7.35). The solution is

$$T - T_{in} = \frac{\alpha}{u k_{eff}} q'' e^{-ux/\alpha} \tag{7.38}$$

Equation (7.38) shows the effect of the propagation of heat flux q'' in the porous structure to the depth of z of the order α/u. That is the boundary condition (7.35) holds when the penetration dept is smaller than the length of the structure. That is

$$\alpha/u < L \tag{7.39}$$

From Equation (7.38), we find the maximum peak temperature difference $T_{max} - T_{in}$, which occur at $z = 0$ surfaces, therefore,

$$T_{max} - T_{in} = \frac{\alpha}{u k_{eff}} q'' \tag{7.40}$$

Combining Equations (7.30) to (7.32), as well as Equations (7.36) and (7.40) together, we, have

$$R = \frac{k_f (T_{max} - T_{in})}{q'' L} \cong \frac{32}{\phi} \left(\frac{d_h}{L} \right)^{-2} Be^{-1} \tag{7.41}$$

where *Be* is the dimensionless pressure number [218] and is defined as:

$$Be = \frac{\Delta P L^2}{\mu \alpha_f} \tag{7.42}$$

and

$$\alpha_f = \frac{k_f}{\rho_f C_{Pf}} \tag{7.43}$$

From Equation (7.41), it can be concluded that in the small diameter extreme, R increases as $d_h \to 0$.

7.8.2. Extreme Limit 2: Large Channel

In this extreme limit, the channels characteristic dimension is sufficiently large in such a way that the working fluid is not properly utilised   and working fluid outside the boundary layers becomes useless and the body is not properly cooled in the downstream. (See Figure (7.19)).

The thermal resistance between the heat flux surface and the channel surface is due to conduction in a square chunk of the solid of dimension w/4. All the other assumptions are still maintained.
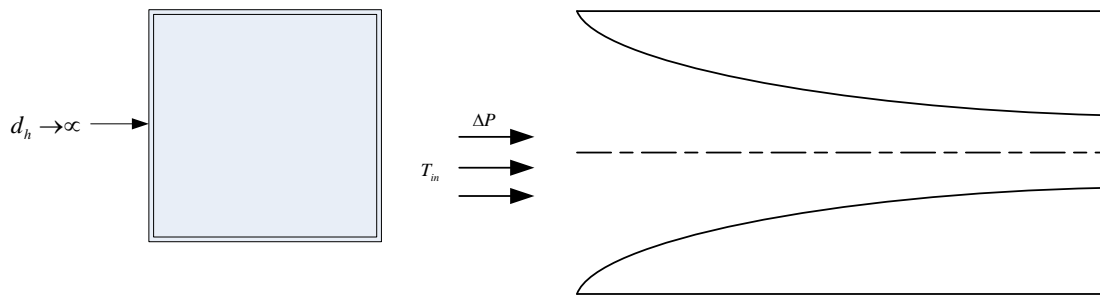

Figure 7. 19 : The extreme limit of the channel's characteristic dimension is sufficiently large, that is $d_h \rightarrow \infty$

The energy equation for describing the steady state conduction in the domain is:

$$\nabla T = 0, \tag{7.44}$$

This requires

$$\nabla T / L_z^2 \, \square \, \nabla T / \left(w/4\right)^2, \tag{7.45}$$

or expects that the path of conduction of heat in the *z* direction should be of the same length scale as the path in the *x* or *y* direction.

$$L_z \, \square \, \frac{w}{4}, \tag{7.46}$$

The conservation of heat current through the elemental volume $L_z \times w/2 \times w/2$,

$$q'' \frac{w}{4} \, \square \, k_s \frac{w}{4} \frac{\Delta T_z}{L_z} \, \square \, k_s L_z \frac{\Delta T_x}{w/4}, \tag{7.47}$$

where, $\Delta T = T - T_{in}$ is temperature difference.

Therefore the overall temperature scale becomes

$$\Delta T \simeq \Delta T_z + \Delta T_x + \Delta T_y \simeq \frac{q''}{k_s}\left(L_z + \frac{w^2}{16L_z} + \frac{w^2}{16L_z}\right), \tag{7.48}$$

combine Equations (7.46) and (7.48) together to get

$$\left(T_{max} - T_{in}\right) \cong 0.75\frac{q''}{k_s}w, \tag{7.49}$$

substitute Equations (7.5) and (7.49) to get

$$\left(T_{max} - T_{in}\right) \cong 0.75\frac{q''}{k_s}\frac{d_h}{\phi^{1/2}}, \tag{7.50}$$

The dimensionless global thermal resistance is defined in terms of dimensionless pressure difference as:

$$R = \frac{k_f\left(T_{max} - T_{in}\right)}{q''L} \cong 0.75 k_r^{-1}\phi^{-1/2}\frac{d_h}{L}, \tag{7.51}$$

From Equation (7.51), it can be concluded that in the large diameter extreme R increases as $d_h \to \infty$.

7.8.3. Optimal Tube Diameter and Spacing

The optimal behaviour of asymptotes can be seen in Figure 7.20 where the fluid is fully utilised. The geometric optimisation in terms of channel hydraulic diameter

could be achieved by combining Equations (7.41) and (7.51) by using the intersection

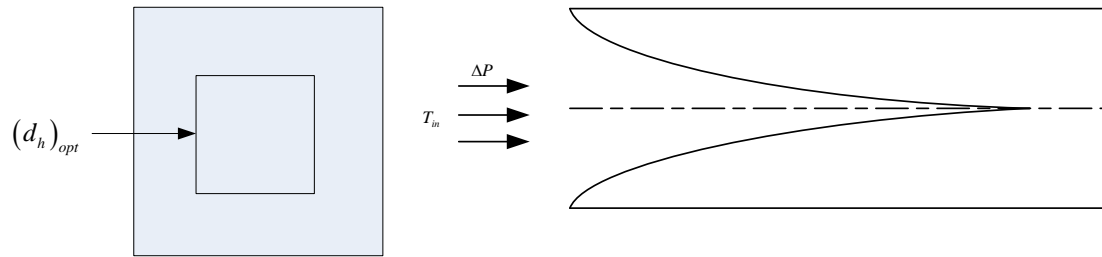of asymptotes method as shown in Figure. 7.21.

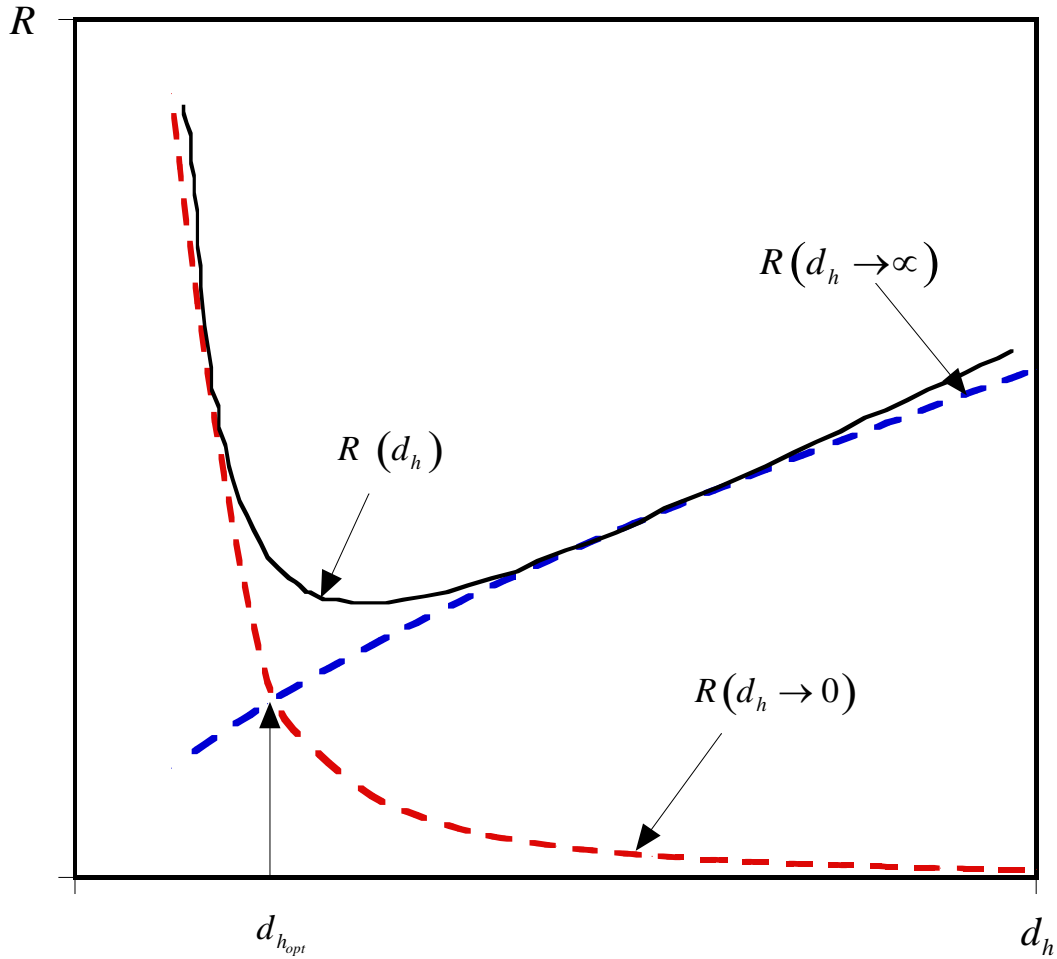**Figure 7. 20 : The optimal limit of the channel's characteristic dimension**

Figure 7. 21 : Intersection of asymptotes Method: Global thermal resistance

The optimal dimension can be generally approximated for the two configurations as the hydraulic diameter where the two extreme curves intersect. The intersection result is

$$\frac{d_{h_{opt}}}{L} \approx 3.494 \phi^{-1/6} k_r^{1/3} Be^{-1/3} \tag{7.52}$$

where $d_{h_{opt}}$ is the optimal hydraulic diameter of the cooling channel.

The optimal spacing s_{opt} between channels follows from Equations (7.3), (7.5) and (7.52), namely

$$\frac{s_{opt}}{L} \approx 3.494 \phi^{-1/6} k_r^{1/3} Be^{-1/3} \left(\phi^{-1/2} - 1 \right) \qquad (7.53)$$

Equations (7.52) and (7.53) show that in the two extremes, the hydraulic diameter and channel spacing decrease as the pressure difference increases for fixed porosity.

The minimum dimensionless global thermal resistance can be obtained for an elemental volume for the configuration that corresponds to the optimal geometries by substituting Equation (7.52) into Equation (7.41) as follows:

$$R_{min} = \frac{k_f \left(T_{max} - T_{in} \right)_{min}}{q'' L} \cong 2.62 \left(k_r \phi \right)^{-2/3} Be^{-1/3}, \qquad (7.54)$$

Equation (7.54) shows that the minimised global thermal resistance decreases monotonically as *Be* increases for a fixed porosity.

The optimisation results of Equations (7.52) and (7.54) agreed within a factor of order of one with the corresponding results obtained by Kim *et al*. [130].

7.9. CORRELATIONS OF THE THEORETICAL METHOD AND NUMERICAL OPTIMISATION

The analytical results of Equations (7.52) to (7.54) were used to validate the numerical solutions. The numerical and approximate solutions based on scale analysis at optimal geometry dimensions are in good agreement and the solutions have similar trends as shown in Figures 7.22 to 7.24.

Figure 7.22 shows the minimised dimensionless global thermal resistance group as a function of the dimensionless pressure difference at optimised design variables for the configuration. The analytical and numerical results show that the minimised global thermal resistance group decreases as the dimensionless pressure difference increases. Figures 7.23 and 7.24 show the effect of the dimensionless pressure difference on the optimised dimensionless design variable groups. The curves show that the optimised design variables decrease as the applied dimensionless pressure difference and porosity increase. This shows that a unique optimal design geometry exists for each applied dimensionless pressure difference, thermal conductivity ratio and porosity.

Furthermore, the optimised channel spacing is directly proportional to the optimised hydraulic diameter. This is due to the fact that the elemental volume is not fixed, but allowed to morph for a fixed porosity. In all cases (objective function and design

variables), the theoretical and numerical values agree within a factor of the order one for the worst case. These results are also in agreement with past research work [130].
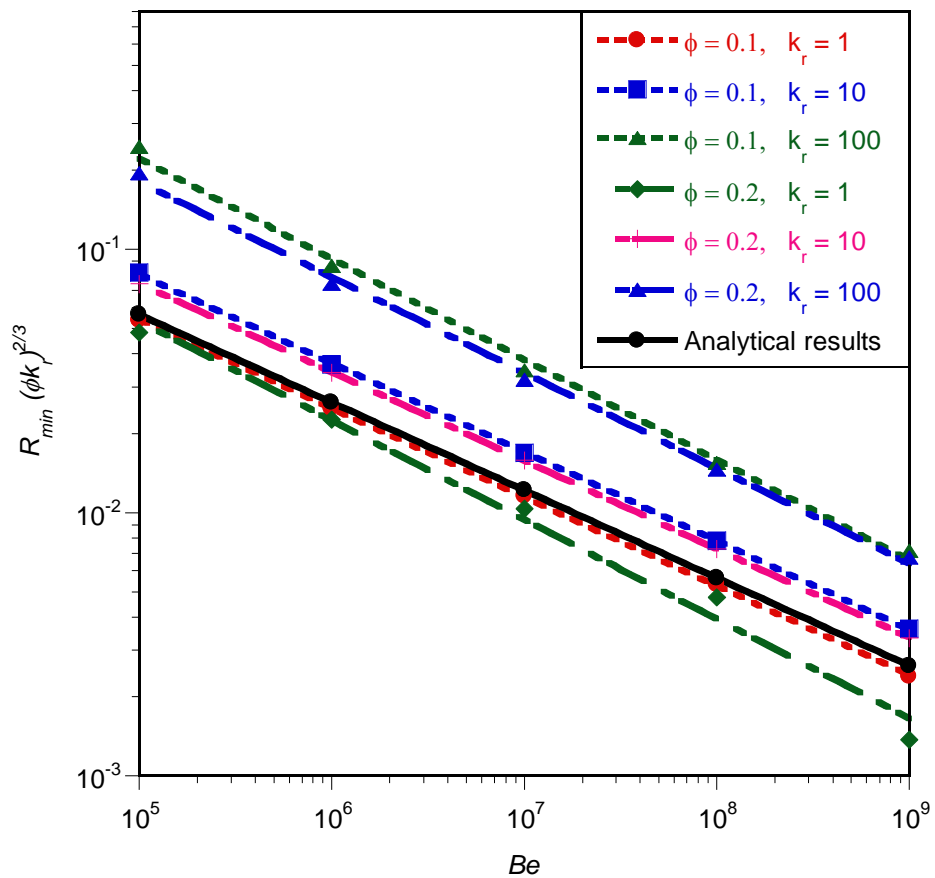

Figure 7. 22 : Correlation of the numerical and analytical solutions for the minimised global thermal resistance
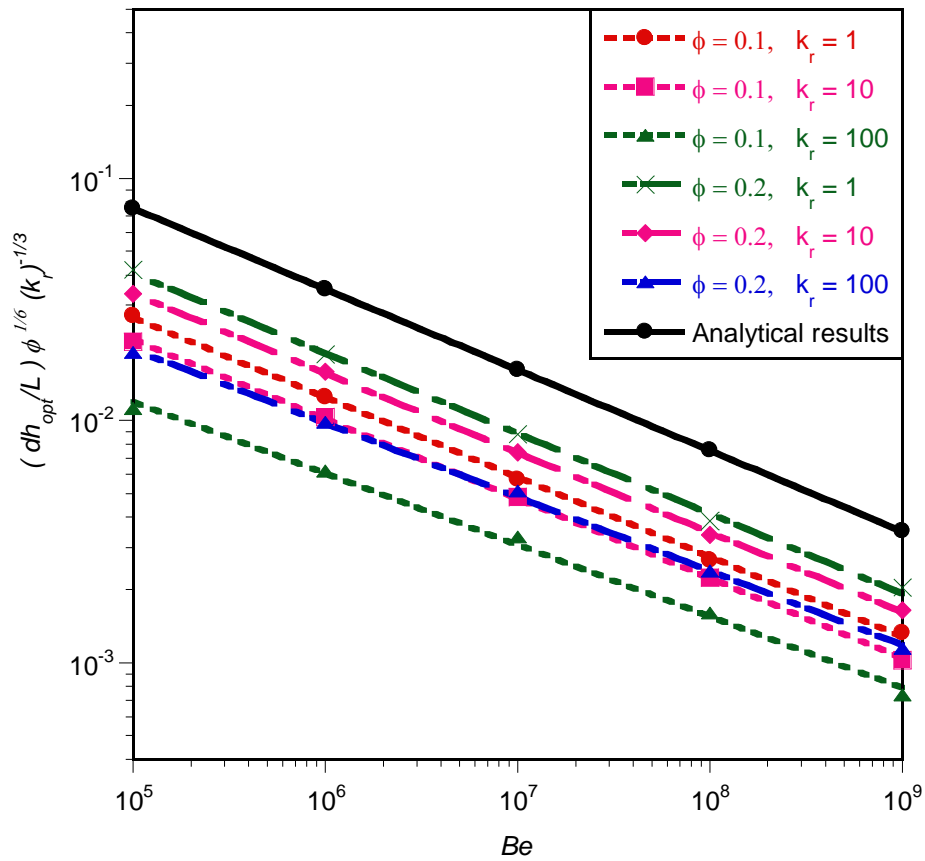
Figure 7. 23 : Correlation of the numerical and analytical solutions for the optimised hydraulic diameter
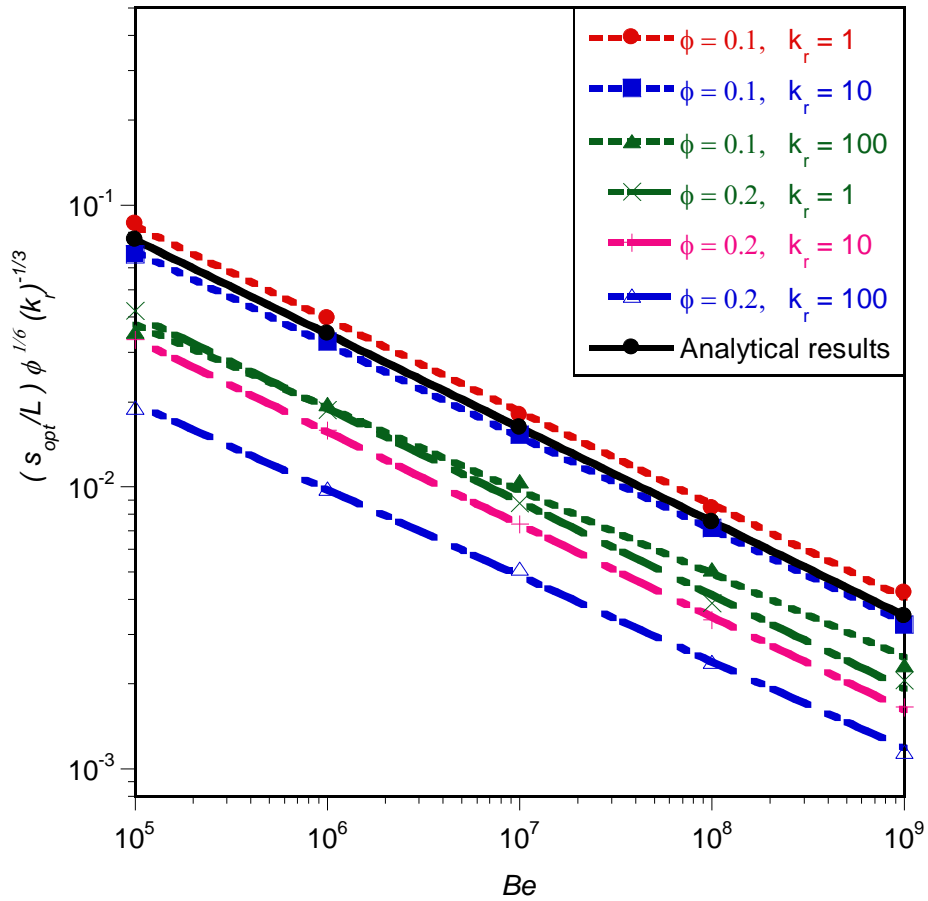
Figure 7. 24 : **Correlation of numerical and analytical solutions for the optimised channel spacing**

7.10. CONCLUSION

This chapter studied the numerical and analytical optimisation of geometric structures for square cooling channels of vascularised material with a localised self-cooling property, subject to a heat flux on one side in such a way that the peak temperature is minimised at every point in the solid body. The numerical results obtained agree well with results obtained in the approximate solutions based on scale analysis at optimal geometry dimensions. The approximate dimensionless global thermal resistance predicts the trend obtained in the numerical results. This shows that there are unique optimal design variables (geometries) for a given applied dimensionless pressure number for fixed porosity. The use of the optimisation algorithm coupled with the CFD package, rendered the numerical results more robust with respect to the selection of optimal structure geometries, internal configurations of the flow channels and dimensionless pressure difference.

The results also show that material property has a significant influence on the performance of the cooling channel. Therefore, when designing the cooling structure of vascularised material, the internal and external geometries of the structure, material properties and pump power requirements are very important parameters to be considered in achieving efficient and optimal designs for the best performance.